4. L. S. Magde *et al.*, *ibid.* **100**, 3747 (1995).
5. M.-H. Cormier, D. S. Scheirer, K. C. Macdonald, *Mar. Geophys. Res.* **18**, 53 (1996).
6. M. A. Eberle, D. W. Forsyth, E. M. Parmentier, *J. Geophys. Res.*, in press.
7. D. S. Scheirer, D. W. Forsyth, M.-H. Cormier, K. C. Macdonald, *Science* **280**, 1221 (1998).
8. C. DeMets, R. G. Gordon, D. F. Argus, S. Stein, *Geophys. Res. Lett.* **21**, 2191 (1994).
9. The MBA is calculated by removing from the free-air anomaly the gravity effect of the water-crust and crust-mantle boundary topography, assuming a 6-km crustal thickness. The east-west asymmetry of ~18 mGal in the MBA across the EPR at ~15°55′S (*7*) can be explained by an east-west decrease in the mantle density of $\Delta\rho \approx 5$ kg/m^3 within the upper 100 km of the mantle. Assuming that the change in density is caused by thermal expansion, an east-west increment in mantle temperature of $\Delta T \approx 50°C$ is required, if the mantle density and the coefficient of thermal expansion are $\rho_m = 3300$ kg/m^3 and $\alpha = 3.1 \times 10^{-5}$ K^{-1}, respectively.
10. J. Willoughby, J. Orcutt, D. Horwitt, *Bull. Seismol. Soc. Am.* **83**, 190 (1993). For a comprehensive overview of the instruments, contact www-mpl.ucsd.edu/obs
11. C. A. Zelt and R. B. Smith, *Geophys. J. Int.* **108**, 16 (1992).
12. S. Bazin *et al.*, *Geophys. Res. Lett.*, in press.
13. Although we find that the best fitting lower crustal velocities are different between the Pacific and Nazca plates, the difference falls within the assigned velocity uncertainty (±0.1 km/s).
14. R. S. Detrick *et al.*, *Science* **259**, 499 (1993).
15. J. G. Mutter *et al.*, *ibid.* **268**, 391 (1995).
16. K. C. Macdonald, J.-C. Sempéré, P. J. Fox, *J. Geophys. Res.* **89**, 6049 (1984).
17. K. C. Macdonald and P. J. Fox, *Earth Planet. Sci. Lett.* **88**, 119 (1988).
18. E. E. Hooft, R. S. Detrick, G. M. Kent, *J. Geophys. Res.* **102**, 27319 (1997).
19. G. A. Barth and J. C. Mutter, *ibid.* **101**, 17951 (1996).
20. J. S. Collier and M. C. Sinha, *Nature* **346**, 646 (1990).
21. ———, *J. Geophys. Res.* **97**, 14031 (1992).
22. G. M. Kent, A. J. Harding, J. A. Orcutt, *ibid.* **98**, 13971 (1993).
23. D. R. Toomey, W. S. D. Wilcock, S. C. Solomon, W. C. Hammond, J. A. Orcutt, *Science* **280**, 1224 (1998).
24. Supported by NSF grant OCE 94-03697 to the Woods Hole Oceanographic Institution. J.P.C. was supported by a Ministerio de Educación y Ciencia (Spain)/Fulbright scholarship (FU96-28992999). Woods Hole Oceanographic Institution contribution number 9707.

17 February 1998; accepted 9 April 1998

Shipboard Geophysical Indications of Asymmetry and Melt Production Beneath the East Pacific Rise Near the MELT Experiment

Daniel S. Scheirer,* Donald W. Forsyth, Marie-Hélène Cormier, Ken C. Macdonald

Near the Mantle Electromagnetic and Tomography (MELT) Experiment, seamounts form and off-axis lava flows occur in a zone that extends farther to the west of the East Pacific Rise than to the east, indicating a broad, asymmetric region of melt production. More seamounts, slower subsidence, and less dense mantle on the western flank suggest transport of hotter mantle toward the axis from the west. Variations in axial ridge shape, axial magma chamber continuity, off-axis volcanism, and apparent mantle density indicate that upwelling is probably faster and more melt is produced beneath 17°15′S than beneath 15°55′S. Recent volcanism occurs above mantle with the lowest seismic velocities.

Using multibeam, swath measurements of bathymetry and sea-floor reflectivity, as well as gravity and magnetic field measurements (*1*), we can map the distribution of seamounts and recent lava flows, determine the detailed geometry and history of the plate boundary, and deduce where there are variations in crustal thickness or mantle density. In addition to providing the context for the design of the MELT Experiment, these observations yield indications of the pattern of mantle flow and melt production beneath the axis that complement those from the seismological observations.

The MELT experiment is centered on a linear, 800-km-long section of the East Pacific Rise (EPR) stretching from the Garrett Transform Fault at ~13.5°S to the large overlapping spreading center (OSC) at 20°40′S (Fig. 1). On a finer scale, the plate boundary is disrupted by a series of small, left-stepping, en echelon discontinuities (*2, 3*) ranging in offset from 1 to ~5 km at the OSC at 15°55′S (Fig. 2). As indicated by subtle variations in sea-floor lava composition, there may be a separate magma source or separate episodes of magma supply for each of the segments separated by these minor discontinuities (*4*). The morphology of the sea floor shows that the OSC locations have changed with time through episodes of rift propagation (*5, 6*). At 17°S, the Pacific (to the west) and Nazca (to the east) Plates are spreading apart at a full rate of 145 mm/year, a fast rate for present-day mid-ocean ridges. Over the past 5 million years, in this area, rapid rift propagation has transferred seafloor from the Pacific to the Nazca Plates, so that the effective sea-floor spreading rate has been on average 10 to 20% faster to the east than to the west (*2, 7, 8*). The combined effects of asymmetric spreading and asymmetric absolute plate motion (Fig. 1) have caused the EPR axis to migrate at about 32 mm/year to the WNW over the hot spot frame of reference in the direction that would tend to keep the spreading center above the regions with the lowest seismic velocities (*9, 10*).

The axis of the spreading center is along a 5- to 20-km-wide ridge (Fig. 2) that stands 200 to 300 m above the background subsidence of the sea floor. On the basis of the gravity anomalies associated with this feature, it has been suggested that this axial topographic high is isostatically supported by low densities in a narrow conduit filled with partial melt, extending tens of kilometers into the mantle (*11–13*). This partial melt zone would correspond to the narrow mantle upwelling center hypothesized in some dynamic models of the spreading process (*14*). However, other models have been suggested for the origin of the axial high that do not require support by buoyant partial melt (*15*).

The axial topographic high is shallower and broader at the latitude of the primary ocean-bottom seismometer (OBS) array than anywhere else in the study area, except for a short, shallow section at about 18°30′S (Figs. 2 and 3). This inflation of the axial ridge is considered to be an indicator of magmatic robustness (*16*). If magma delivery to the crust is not uniform along-axis, inflated areas may lie above centers of upwelling and melt production. Another indication of the overall magma supply, as well as the thermal state of the crust and uppermost mantle, is the mantle Bouguer gravity anomaly (MBA) (*17*). The dominant feature in the MBA is the increase away from the spreading center that is caused by cooling and contraction of the lithosphere with increasing age (Fig. 2B). The lowest values occur where the primary OBS array crosses the ridge, indicating that either the crust is slightly thicker there or the crust and mantle have lower densities. Axial MBA values increase to the north of 17°S and to the south of 18°30′S, reflecting either denser, colder mantle or a decrease in magma supply, leading to thinner crust (the differences could be explained by crust about 400 m thinner near

D. S. Scheirer and D. W. Forsyth, Department of Geological Sciences, Box 1846, Brown University, Providence, RI 02912, USA.
M.-H. Cormier, Lamont-Doherty Earth Observatory of Columbia University, Palisades, NY 10964, USA.
K. C. Macdonald, Department of Geological Sciences, University of California, Santa Barbara, CA 93106, USA.

*To whom correspondence should be addressed. E-mail: scheirer@emma.geo.brown.edu

the 15°55′S OSC). Wang and Cochran (*12*) suggested that, along another section of the EPR, concentrated upwelling or magma was centered at the location of the lowest MBA.

If magma is delivered to a central portion of the ridge axis and then redistributed along-axis at crustal levels, magma chambers could play an important role in the redistribution. In seismic reflection data, a strong event lies about 0.8 to 2.0 km beneath the spreading axis and marks the top of an axial magma chamber (AMC) that is less than 100 m thick and up to 1 km wide (*18–20*). Along this portion of the southern EPR, the AMC reflector is present and nearly continuous (Fig. 3), except for an ~100-km-long section extending from about 40 km north of the 15°55′S OSC to the 16°30′S OSC (*18*). The absence of an AMC is another indication of a less robust or less recent supply of melt to the ridge.

South of about 15.8°S, there are broad isotopic compositional anomalies in basalt samples from the EPR (Fig. 3), indicating that the normal mantle that generates mid-ocean ridge basalts is contaminated by mantle with a plume or hot spot isotopic signature (*21, 22*). The maximum lead, strontium, and neodymium isotopic anomalies are displaced significantly to the south of the maximum helium anomaly (Fig. 3), which suggests upwelling near the northern end of the anomalies with subsequent man-

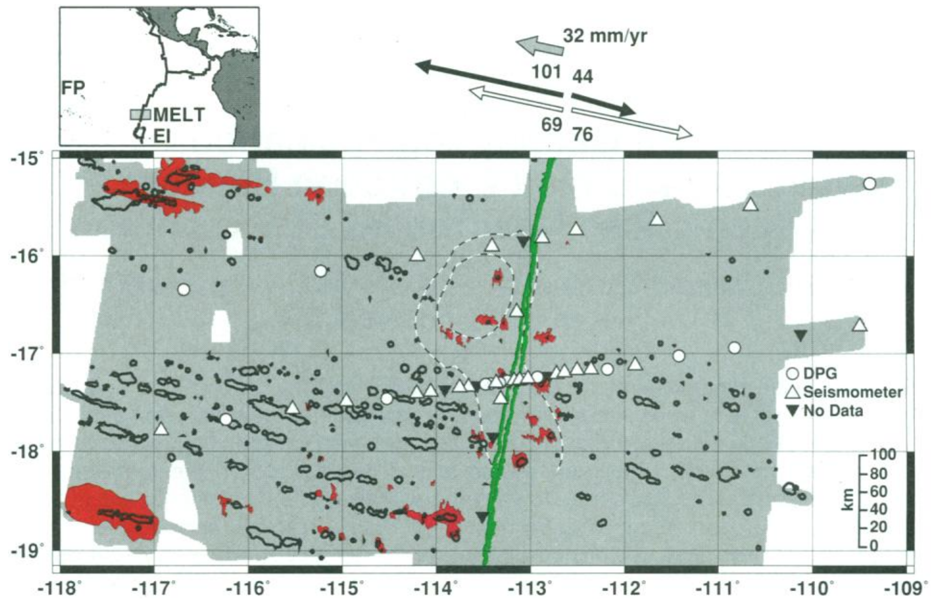

Fig. 1. Distribution of seamounts and recent lava flows on the flanks of the EPR. Gray area indicates extent of bathymetry and side-scan sonar coverage. Black lines enclose seamounts 400 m and higher, and red areas indicate regions of highly reflective seafloor corresponding to recent lava flows. Absolute and relative plate motion vectors are shown by black and white arrows, respectively. Relative plate motion velocities are averages for this area over the past 5 million years; asymmetric spreading varies significantly for smaller areas or time intervals. Thick gray arrow represents average motion of the ridge axis relative to the hot spot frame of reference over this time interval. Circles and triangles indicate locations of OBSs in the MELT arrays. Green line is the 2800-m depth contour that delimits the axial ridge. Dashed lines indicate the 3.69 km/s (inner) and 3.70 km/s (outer) contours defining the lowest Rayleigh wave-phase velocities from a tomographic inversion of Forsyth *et al.* [figure 3B in (*9*)]. (Inset) Study area in the eastern Pacific Ocean; FP, French Polynesia; EI, Easter Island.

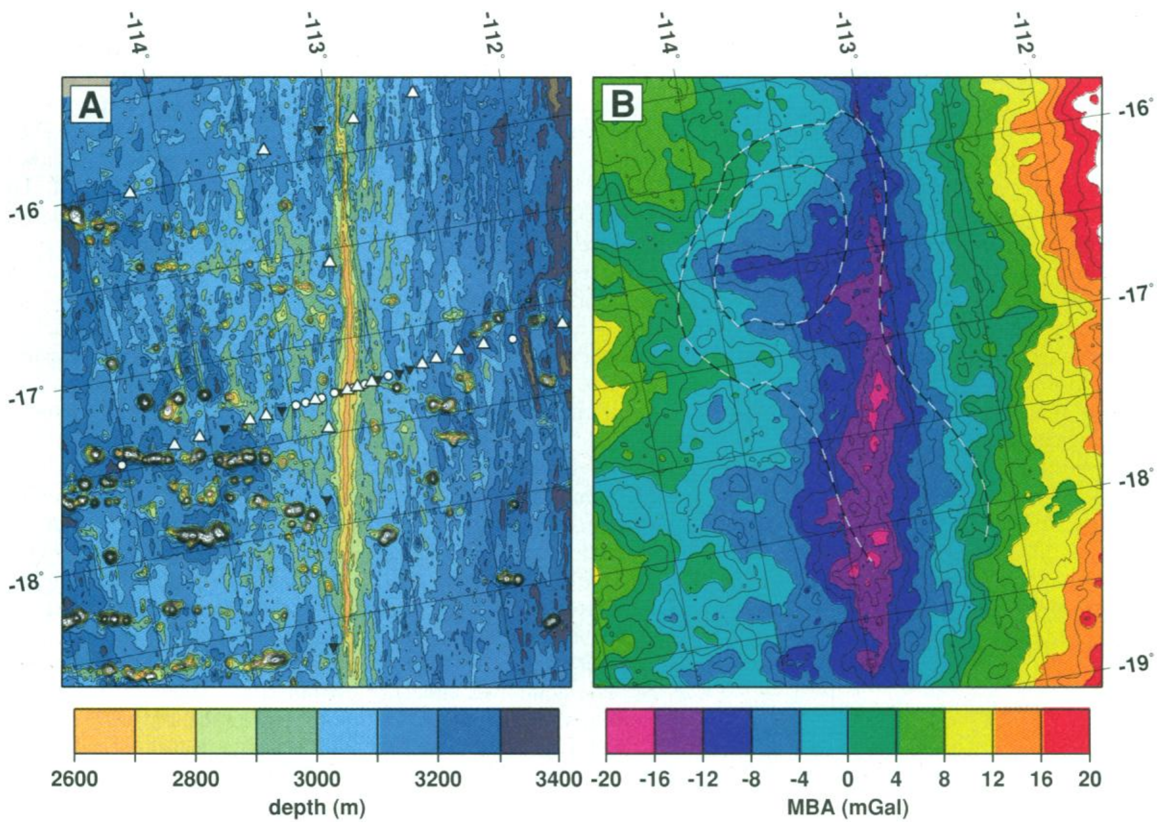

Fig. 2. (**A**) Bathymetry of the ridge axis contoured every 100 m. The oblique projection extends about 140 km to the east and 180 km to the west of the southern EPR out to crustal ages of about 1.8 and 2.5 Ma, respectively. (**B**) MBA, contoured every 2 mGal with color changes every 4 mGal. Cool colors indicate negative MBAs, corresponding to relative low densities; warm colors indicate positive MBAs and high densities. Dashed lines are phase velocity contours described in Fig. 1.

tle flow toward the south (*21*). The coincidence of the minimum Rayleigh wave velocities (9) and the lowest off-axis mantle Bouguer anomalies to the west of the axis at about this latitude (Fig. 2B) may indicate that the heterogeneity is displaced to the Pacific Plate side.

From the Wilkes Transform (9°S) to the Easter Microplate (23°S), the Pacific flank subsides at about half the rate of the Nazca flank and of the global average (*23*). In the MELT area, this asymmetry is pronounced (Fig. 2A); at 1 million years ago (Ma), average Nazca sea floor is about 100 m deeper than Pacific sea floor, and at 4 Ma this difference is nearly 300 m. The free-air anomaly and geoid height have no significant across-axis gradient in this region, which indicates that the seafloor is in isostatic equilibrium and that the difference in subsidence rate stems from a difference in mantle densities and not from the superposition of a dynamically supported topographic gradient on symmetric thermal subsidence. The asymmetry is probably created primarily by asymmetric upper mantle temperatures (*23*, *24*), possibly generated by hotter mantle in the asthenosphere flowing in from the west from the superswell region (*25*, *26*) of the French Polynesian hot spots (Fig. 1). However, the isotopic anomalies of lavas erupted at the southern EPR have closer chemical affinity to Nazca hot spots than to the superswell hot spots (*27*), indicating that they arise from a localized mantle heterogeneity or upwelling anomaly rather than from direct transport of hot spot material from the plumes to the west.

The asymmetry across the ridge is even more obvious in the MBA map (Fig. 2B). The asymmetric MBA reflects the isostatically compensated, asymmetric subsidence and is produced by subtracting the effects of asymmetric topography from a symmetric, nearly flat free-air gravity anomaly. In some places, the asymmetry is enhanced by local anomalies associated with seamounts, probably generated by a thickening of the extrusive layer of the crust beneath and adjacent to the seamounts, in addition to the added crustal volume of the seamount edifice itself (*28*, *29*). The lowest MBA values off-axis at about 16°30′S lie in a region with only very small seamounts (Fig. 2), although there are some fresh off-axis flows nearby (Fig. 1). It is clear that seamounts and their associated crustal thickening are not responsible for the fundamental asymmetry in mantle densities revealed by the MBA.

Seamount formation and recent lava flows provide another direct indication of melt production and transport to the surface. Although 98 to 99% of the volume of the crust is created within 1 or 2 km of the ridge axis (*30*, *31*), delivery of some melt off-axis creates seamounts and low-relief lava flows (Fig. 1). Many seamounts form in a zone 5 to 50 km from the southern EPR axis on either plate, and no seamounts form on the axis itself (*31*) (Fig. 2A). There are far more seamounts between 17° and 19°S in the Rano Rahi seamount field than between 15° and 17°S, and seamounts are more common on the western than on the eastern flank (Figs. 1 and 2A). Although most of the recent, off-axis lava flows occur within 60 km of the axis, on the west side, the continued growth in population and volume of seamounts with increasing distance from the axis and the occurrence of highly reflective flows indicate some melt production extending more than 100 km from the axis. In the latitude range with good Rayleigh wave tomographic resolution, the locations of recent off-axis flows correspond fairly well with the region of lowest phase velocity (Fig. 1), which is expected to define the area of greatest melt in the mantle.

Wilson (*11*) interpreted the absence of seamounts on the spreading axis and the production of seamounts in a finite-width zone on the flanks as indicating (1) narrow upwelling of the mantle to generate the melt feeding the axis and (2) deep melting of small-volume mantle heterogeneities and subsequent melt ascent outside this main upwelling zone to form the seamounts. In analogy with the model of Davis and Karsten (*33*), the motion of the southern EPR toward the west-northwest in the absolute (hot spot) reference frame might lead to the formation of seamounts preferentially to the west of the axis (as is observed) if more easily melting mantle heterogeneities are the ultimate source of the seamount magmatism.

If, on the other hand, the zone of mantle feeding the axis is broad, then the mechanism that focuses melt toward a narrow axial zone of eruption must leak to allow some vertical ascent of melts to form off-axis seamounts (*34*, *35*). Melts formed close to the axis may be efficiently transported to the spreading center and then redistributed in the axial magma chamber, so that no seamounts form on-axis. Fast mantle upwelling and significant melt production may continue beneath the flanking regions where most seamounts are formed and recent off-axis flows are found (*36*). Thickening of the lithosphere with distance from the axis also may make it more difficult for melts to propagate to the surface, thus limiting the extent of off-axis volcanism. To produce the asymmetry in seamount population with broad mantle upwelling requires an asymmetry in some properties of the lithosphere or underlying asthenosphere, such as higher temperatures or more abundant compositional heterogeneities.

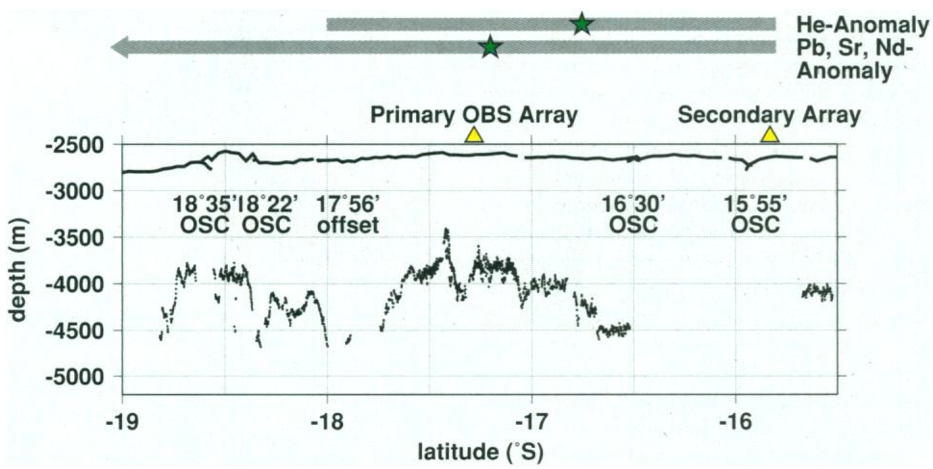

Fig. 3. Along-axis variations in spreading-center depth (solid line) and depth to the top of the axial magma chamber reflector (dots) (*37*). Locations of the isotopic anomalies from basalt samples (*21*) are indicated as bars, and the anomaly maxima are displayed as stars.

REFERENCES AND NOTES

1. In this paper, new data from cruises BMRG01MV, TN061, and SOJN01MV provide coverage of the east flank of the EPR and fill in gaps in the prior coverage.
2. P. Lonsdale, *J. Geophys. Res.* **94**, 12197 (1989).
3. D. S. Scheirer, *et al.*, *Mar. Geophys. Res.* **18**, 1 (1996).
4. J. M. Sinton, S. M. Smaglik, J. J. Mahoney, K. C. Macdonald, *J. Geophys. Res.* **96**, 6133 (1991).
5. M.-H. Cormier and K. C. Macdonald, *ibid.* **99**, 543 (1994).
6. M.-H. Cormier *et al.*, *Eos Fall Suppl.* **77**, 660 (1996).
7. D. F. Naar and R. N. Hey, in *Evolution of Mid-Ocean Ridges*, J. M. Sinton, Ed. (American Geophysical Union, Washington, DC, 1989), pp. 9–30.
8. M.-H. Cormier, D. S. Scheirer, K. C. Macdonald, *Mar. Geophys. Res.* **18**, 53 (1996).
9. D. W. Forsyth, S. C. Webb, L. M. Dorman, Y. Shen, *Science* **280**, 1235 (1998).
10. D. R. Toomey *et al.*, *ibid.*, p. 1224.
11. D. S. Wilson, *Earth Planet. Sci. Lett.* **113**, 41 (1992).
12. X. Wang and J. R. Cochran, *J. Geophys. Res.* **98**, 19505 (1993).
13. L. S. Magde *et al.*, *ibid.* **100**, 3747 (1995).
14. W. Su and W. R. Buck, *ibid.* **98**, 12191 (1993).
15. M. A. Eberle and D. W. Forsyth, *ibid.*, in press.

16. D. S. Scheirer and K. C. Macdonald, *ibid.* **98**, 7871 (1993).
17. MBAs are calculated by subtracting from the free-air anomaly the gravitational attraction of sea-floor topography and Moho relief that is assumed to parallel the sea floor (except that the Moho does not shoal beneath seamounts). If crust has a constant density and thickness and the mantle density is constant, then the MBA will be constant.
18. R. S. Detrick *et al.*, *Science* **259**, 499 (1993).
19. J. C. Mutter *et al.*, *ibid.* **268**, 391 (1995).
20. S. A. Hussenoeder *et al.*, *J. Geophys. Res.* **101**, 22087 (1996).
21. J. J. Mahoney *et al.*, *Earth Planet. Sci. Lett.* **121**, 173 (1994).
22. W. Bach, E. Hegner, J. Erzinger, M. Satir, *Contrib. Miner. Petrol.* **116**, 365 (1994).
23. J. R. Cochran, *Geophys. J. R. Astron. Soc.* **87**, 421 (1986).
24. M.-H. Cormier, K. C. Macdonald, D. S. Wilson, *J. Geophys. Res.* **99**, 8063 (1995).
25. M. K. McNutt and A. V. Judge, *Science* **248**, 969 (1990).
26. J. Phipps Morgan, W. J. Morgan, Y.-S. Zhang, W. H. F. Smith, *J. Geophys. Res.* **100**, 12753 (1995).
27. L. S. Hall and J. M. Sinton, *Eos* **77**, 660 (1996).
28. J.-G. Schilling, D. Fontignie, R. Kingsley, in *Mantle Flow and Melt Generation Beneath Mid-Ocean Ridges, Program with Abstracts* (RIDGE, Providence, RI, 1997); Hall *et al.*, *Eos* **77**, 660 (1996).
29. J. P. Canales, R. S. Detrick, S. Bazin, A. J. Harding, J. A. Orcutt, *Science* **280**, 1218 (1998).
30. S. Bazin *et al.*, *Geophys. Res. Lett.*, in press.
31. D. S. Scheirer, K. C. Macdonald, D. W. Forsyth, Y. Shen, *Mar. Geophys. Res.* **18**, 13 (1996).
32. Y. Shen, D. W. Forsyth, D. S. Scheirer, K. C. Macdonald, *J. Geophys. Res.* **98**, 17875 (1993).
33. E. E. Davis and J. L. Karsten, *Earth Planet. Sci. Lett.* **79**, 385 (1986).
34. R. Batiza and D. Vanko, *J. Geophys. Res.* **89**, 11260 (1984).
35. Y. Niu and R. Batiza, *ibid.* **96**, 21753 (1991).
36. The large, recently active seamounts in the westernmost part of the study area (Fig. 1) are probably created by a mechanism that is distinct from the normal upwelling associated with the EPR, such as small-scale convection or local stretching of the Pacific Plate.
37. E. E. E. Hooft, R. S. Detrick, G. M. Kent, *J. Geophys. Res.* **102**, 27319 (1997).
38. We thank R. Batiza, an anonymous reviewer, and the other MELT investigators for comments that improved this paper. Supported by NSF grants OCE-9402375 and OCE-9615204.

18 February 1998; accepted 21 April 1998

Mantle Seismic Structure Beneath the MELT Region of the East Pacific Rise from *P* and *S* Wave Tomography

Douglas R. Toomey,* William S. D. Wilcock, Sean C. Solomon, William C. Hammond, John A. Orcutt

Relative travel time delays of teleseismic *P* and *S* waves, recorded during the Mantle Electromagnetic and Tomography (MELT) Experiment, have been inverted tomographically for upper-mantle structure beneath the southern East Pacific Rise. A broad zone of low seismic velocities extends beneath the rise to depths of about 200 kilometers and is centered to the west of the spreading center. The magnitudes of the *P* and *S* wave anomalies require the presence of retained mantle melt; the melt fraction near the rise exceeds the fraction 300 kilometers off axis by as little as 1%. Seismic anisotropy, induced by mantle flow, is evident in the *P* wave delays at near-vertical incidence and is consistent with a half-width of mantle upwelling of about 100 km.

Competing models for mantle flow and for the generation and transport of melt beneath mid-ocean ridges (*1*) predict detectable differences in mantle seismic structure. The travel times of body waves from distant earthquakes, recorded by an ocean-bottom array of sensors, should be sensitive to the distribution of melt retained in the mantle and to seismic anisotropy produced by flow-induced finite strain (*2*). Here, we report an analysis of body-wave travel time delays from the MELT Experiment (*3*) on the southern East Pacific Rise (EPR) and their implications for the seismic structure and mantle flow pattern beneath a fast-spreading oceanic ridge.

From a subset of the MELT network (*3*), we measured 500 relative delay times of filtered *P* and *S* waves from 20 earthquakes at epicentral distances greater than 30°. *P* waves were easily identified on the vertical seismometer at frequencies between 0.14 and 0.5 Hz, equivalent to an average seismic wavelength in the mantle of about 35 km (*4*). Shear waves were also observed on horizontal seismometers with good signal-to-noise ratios at frequencies of 0.05 to 0.1 Hz (average upper-mantle seismic wavelength of about 70 km). Because shear wave splitting is observed (*5*), *S* waves polarized in the fast (S_{fast}) and slow (S_{slow}) directions, respectively subparallel and subperpendicular to the spreading direction, were analyzed independently (*6*). For both types of body waves, arrivals are coherent at nearby stations, allowing us to use cross-correlation methods (*7*) to improve the accuracy of estimated delay times (*8*). All delays, measured relative to a standard Earth model (*9*), have had a mean value removed for each event.

Mean *P*-wave delay times in the frequency band 0.14 to 0.5 Hz vary by ~0.7 s across the network; the greatest delays are on and near the rise axis (Fig. 1A). Along the primary ocean bottom seismometer (OBS) array (*3*), the cross-axis delay time pattern is asymmetric. At similar crustal ages, delays to the west are consistently greater by 0.1 to 0.2 s than those to the east; this asymmetry is evident within 5 to 10 km of the rise axis. The cross-axis pattern is not well constrained along the secondary OBS

D. R. Toomey and W. C. Hammond, Department of Geological Sciences, University of Oregon, Eugene, OR 97403, USA.
W. S. D. Wilcock, School of Oceanography, University of Washington, Seattle, WA 98195, USA.
S. C. Solomon, Department of Terrestrial Magnetism, Carnegie Institution of Washington, Washington, DC 20015, USA.
J. A. Orcutt, Institute of Geophysics and Planetary Physics, Scripps Institution of Oceanography, University of California at San Diego, La Jolla, CA 92093, USA.

*To whom correspondence should be addressed. E-mail: drt@newberry.uoregon.edu

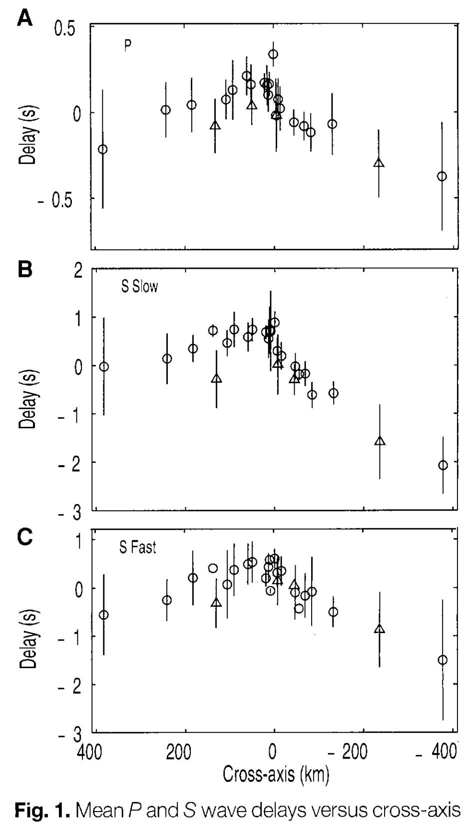

Fig. 1. Mean *P* and *S* wave delays versus cross-axis distance. Circles and triangles denote sites along the primary and secondary OBS arrays (*3*), respectively. Vertical bars indicate standard deviations in observed delays at a given site; uncertainties in individual delays are considerably smaller, ~0.1 s for *P* and 0.3 s for *S*. (**A**) *P* delay; (**B**) S_{slow} delay; (**C**) S_{fast} delay. The S_{slow} and S_{fast} directions, defined by the shear wave splitting analysis (*5*), are approximately subparallel to the rise and spreading directions, respectively.